Supporting Information

Strüber et al. 10.1073/pnas.1412996112

SI Materials and Methods

Electrophysiology and Solutions. Acute hippocampal slices were superfused in an artificial cerebrospinal fluid consisting of the following (in mM): 125 NaCl, 25 $NaHCO_3$, 2.5 KCl, 1.25 NaH_2PO_4, 25 D-glucose, 2 $CaCl_2$, and 1 $MgCl_2$ (equilibrated with 95% O_2/5% CO_2) for 30 min (34 °C) and then stored at room temperature. Recording pipettes (wall thickness: 0.5 mm; inner diameter: 1 mm) were pulled from borosilicate glass tubing (Hilgenberg; Flaming-Brown P-97 puller; Sutter Instrument) and filled with a solution containing the following (in mM): 110 K-gluconate, 40 KCl, 10 Hepes, 2 $MgCl_2$, 2 Na_2ATP, 0.1 EGTA, and 0.1% biocytin (Molecular Probes) (pH 7.2; 290–310 mOsm). Pipette resistance was 2.5–5 MΩ. Patch-clamp recordings were performed with two Axopatch 200B amplifiers. Signals were filtered at 5–10 kHz and digitized at 20–40 kHz with a Power1401 laboratory interface (Cambridge Electronic Design). Series resistance (7–20 MΩ) was compensated in voltage clamp at 75–90%, with 10- to 40-μs time lag. Igor-based programs (FPulse 3.33, custom-made; U. Fröbe, University of Freiburg, Freiburg, Germany) were used for stimulus generation and data acquisition.

Paired recordings were performed only from cells located >60 μm from the slice surface. Single action potentials were evoked by brief depolarizing current injection in the PII and uIPSCs were recorded (−70-mV holding potential) in the postsynaptic GC (recording temperature: 30–34 °C). For multiple sequential paired recordings, the pipette was subsequently removed from the GC and the next GC was recorded. This procedure was repeated up to 10 times in a spatially randomized fashion. Only GCs with input resistance <500 MΩ (resting membrane potential, −70 to −85 mV) were used for analysis. PIIs displayed a fast-spiking (maximal firing frequency, >100 Hz), nonadapting discharge pattern and had axons located predominantly in the GC layer. In five out of five morphologically and physiologically identified PIIs, PV expression was verified by antibody labeling (Swant; polyclonal rabbit anti-PV).

Morphological Analysis. After completing electrophysiological recordings, slices were fixed [in 4% paraformaldehyde in 100 mM phosphate buffer (PB) for fluorescence staining or 2.5% paraformaldehyde, 1.25% glutaraldehyde, and 15% saturated picric acid in 100 mM PB for peroxidase staining (all concentrations given in vol/vol)], and biocytin-filled cells were visualized using either streptavidin conjugated to Alexa Fluor 488 or Alexa Fluor 647 (1:500; Invitrogen), or avidin–biotinylated horseradish peroxidase complex and 3,3′-diaminobenzidine as chromogen. Neurons with axonal arborizations confined to the principal cell layer (~80%; Fig. 1*A*) were identified as perisoma-inhibiting interneurons (PIIs), which comprise basket and axo-axonic cells (1, 2). According to previous morphological analysis, the abundance of PV-expressing axo-axonic cells in our sample was likely to be small (3). We carefully investigated the axonal arbors of the recovered PIIs by analyzing confocal image stacks or using light microscopy. Experiments were discarded if major damages to the axonal arbor (e.g., due to the slicing procedure) were observed.

To investigate morphological correlates of PII–GC connections, postsynaptic GCs were intracellularly filled with 2 mM Lucifer Yellow CH (Life Technologies), and the axonal length and location as well as number of putative synapses were analyzed in a post hoc manner. Putative morphological synaptic contacts were defined as close appositions of the PII axon to the somatodendritic domains of GCs in labeled PII–GC pairs. The postsynaptic dendritic distance of a synaptic connection was the average of all somatodendritic distances from the putative synaptic contacts to the center of the postsynaptic soma (Fig. S1*A*). To estimate the axonal distance of PII–GC connections (Fig. 1*C*), the axon was reconstructed from the beginning of the axon initial segment to the putative synaptic contacts (Simple Neurite Tracer plugin, Fiji based on ImageJ 1.47g), and the average of all axonal distances was calculated. In some PIIs, the axon initial segment originated not at the soma but from the main apical dendrite, presumably delaying the action potential initiation upon somatic current injection. We therefore excluded PIIs from our sample when the axon initial segment originated at dendritic distances >60 μm.

Data Analysis. Functional properties of uIPSCs were quantified on the basis of average uIPSCs from 30 to 60 traces. The rise time of average uIPSCs was determined as the time interval between the points corresponding to 20% and 80% of the peak amplitude, respectively. Alternatively, the average of the rise times of individual uIPSCs was calculated. In both cases, the rise time did not correlate with synaptic latency ($P = 0.383$ vs. $P = 0.948$, respectively). Synaptic latency was determined as the time interval between the maximum of the first derivative of the presynaptic action potential and the onset of the average uIPSC. Axonal distance was either measured directly after morphological tracing of the axon (seven reconstructed pairs) or calculated from the latency–distance relation (Fig. 1*C*). The decay phase of IPSCs was fit with the sum of two exponentials $[A_1 \exp(-t/\tau_1) + A_2 \exp(-t/\tau_2)]$, using a nonlinear least-squares fit algorithm; time constants are reported as an amplitude-weighted mean $[\tau = (A_1 \tau_1 + A_2 \tau_2)/(A_1 + A_2)]$. A trace was classified as a failure if the peak amplitude was less than three times the SD of the baseline. Membrane potentials were not corrected for junction potentials.

We describe the relation between amplitude (amp) or τ and distance by the distance-dependence (dd) coefficients α and β. These factors result from the declining exponential (α) or linear (β) functions that fit the pooled data from paired recordings best (Fig. 1*D*). These fit functions are as follows:

$$\mathrm{amp}(\mathrm{distance}) = \mathrm{amp}_0 \cdot \exp(-\alpha \cdot \mathrm{distance}), \quad \textbf{[S1]}$$

$$\tau(\mathrm{distance}) = \tau_0 + \beta \cdot \mathrm{distance}. \quad \textbf{[S2]}$$

The factors α and β are 0.006 μm^{-1} and 0.012 $ms \cdot \mu m^{-1}$ in the spatial dimension, and 1.7 ms^{-1} and 3.6 $ms \cdot ms^{-1}$ in the temporal dimension.

In Fig. S2, we directly compare distance-dependence in amp, τ, and rise time of uIPSCs obtained from single sets of sequential paired recordings (SPRs). To statistically test the relation of these functional properties to axonal distance of individual presynaptic PIIs, we fit the relationship between, e.g., amplitude and difference in axonal distance for every SPR individually with a linear function and obtained 12 separate slopes m_i for the 12 SPRs.

In some SPRs, only two and in others four subsequent paired recordings have been established. With increasing cell numbers in each SPR, a better estimate on the relation between synaptic properties and distance can be deduced. To account for this variability, we weighted the slopes of the linear functions from 12 SPRs by the number of postsynaptic cells and the distance range of every SPR. Thus, the average for the weighted linear fits (μ_n) of all SPRs was determined as follows:

$$\mu_n = \sum m_i \cdot w_i / N \quad \text{with} \qquad \text{[S3]}$$

$$w_i = W_i \Big/ \sum W_i, \qquad \text{[S4]}$$

where W_i is the product of the number of postsynaptic cells in the ith SPR with the covered axonal distance range.

This average describes the average change in the IPSC property (amplitude, τ, rise time) as a function of the difference in axonal distance. The obtained relationship μ_n was statistically tested against the null hypothesis ($\mu_0 = 0$) using a one-sample t test. The SD of the weighted data was calculated with the following equation:

$$\mathrm{SD}^2 = (N-1)^{-1} \sum ((m_i \cdot w_i) - \mu_n)^2. \qquad \text{[S5]}$$

Determination of Quantal Release Characteristics (N_{rs}, p_{rs}, q, and RTC). In a subset of six PII–GC pairs, a high number (range: 30–1,200 traces) of uIPSCs was recorded in normal and low extracellular Ca^{2+} concentration (2 mM Ca^{2+}/1 mM Mg^{2+} and 0.5 mM Ca^{2+}/2.5 mM Mg^{2+}, respectively). The resulting unbinned peak amplitude distributions including failures were fit with a multiple probability–compound binomial analysis (MP-CBA) model of release consisting of the sum of N_{rs} Gaussian functions representing 1 to N_{rs} individual independent release sites (4) (Fig. 2 *A* and *B*). The contribution of individual components is given by the binomial distribution characterized by N_{rs} and p_{rs}. The Gaussian function representing the activation of a single release site is given by mean q and its SD (q_{SD}) (intrasite variability). To reduce the number of free parameters, the intersite variability in quantal amplitude and release probability were assumed to be 0. For the five free parameters (N_{rs}, $p_{rs\ 0.5}$, $p_{rs\ 2}$, q, q_{SD}) initial boundaries were specified: $1 \le N_{rs} \le 20$; $0.01 \le p_{rs\ 0.5} \le 0.40$ (0.5 mM Ca^{2+}) and $0.30 \le p_{rs\ 2} \le 0.80$ (2 mM Ca^{2+}); 10 pA $\le q \le$ 60 pA; 1 pA $\le q_{SD} \le$ 25 pA. The best fit of the data (Fig. 2*A*) was determined with the maximum-likelihood estimation procedure. The transmitter release time course (RTC) at PII–GC synapses (Fig. 2*C*) was determined from first-latency distributions obtained from experiments in the reduced release probability condition at 0.5 mM Ca^{2+}. These first-latency distributions were corrected either with the Barrett and Stevens (BS) (5) approach or using the method described by Minneci et al. (MS) (6). The latter method requires estimates on N_{rs}, which we obtained from the MP-CBA. RTCs were fit with a γ distribution (7) and reconvolved with the average quantal IPSC recorded in the same pair to confirm validity of the computed RTC (Fig. 2*C*).

Imaging of Presynaptic Ca^{2+} Transients. PIIs in acute slices were intracellularly filled with 100 μM OGB-1 and 1 mg·mL^{-1} biocytin [intracellular solution (in mM): 115 K-gluconate, 20 KCl, 10 Hepes, 2 $MgCl_2$, 4 K_2ATP, 10 Na_2-phosphocreatinine (pH 7.2) (8)] for 2–4 h before imaging to ensure homogeneous dye concentration. Then, somatic action potentials were elicited and line scans of morphologically identified putative boutons in various distances were taken with a Femtonics 2D two-photon microscope coupled to a Coherent Chameleon Ultra Ti:Sapphire Laser tuned to 800 nm. For line scans targeting individual presynaptic PII boutons in various distances, laser intensity was generally 2–8% depending on the depth but not higher than 15% to avoid photodamage (sampling frequency, 0.4–1 kHz). Three individual traces were averaged, normalized to baseline, and the average trace was used to determine peak amplitude and decay time constant. The decay time constant was obtained from a monoexponential fit of the decay phase. The baseline noise of the individual recordings was defined as the SD of the Ca^{2+} signal recorded in a 600- to 1,000-ms time window before the evoked action potentials. The values given in Fig. S5 are averages from at least three transients. Only optical traces with a stable baseline and favorable signal-to-noise ratio (peak/baseline SD > 2.5) were included in the analysis. Every somatic action potential induced a Ca^{2+} transient in the recorded boutons demonstrating the high efficiency of the PII axon in spike propagation (9). Distances between recording site and soma were based on a straight 3D connecting line. To exclude artifacts due to inhomogeneous loading of the axon with the dye, only cells were included that showed no correlation of the baseline fluorescence variance with distance. This parameter is highly sensitive to differences in the Ca^{2+} indicator concentration (10).

Immunofluorescence Labeling Against $GABA_A$ Receptor Subunits and Quantification of Their Expression in PII Synapses. Individual PIIs were intracellularly filled with 3 mg·mL^{-1} biocytin for 30 min. After an additional 60-min period of diffusion, slices were fixed in 4% paraformaldehyde for 80 min. Slices were washed in 0.1 M PBS and kept for 60 min in 0.1 M PBS containing 10% normal goat serum (NGS) and 0.2% Triton X-100. Primary antibodies [polyclonal rabbit anti-α1-subunit (1:1,000; gift from Prof. J.-M. Fritschy, University of Zürich); see Gao et al. (11) and Patrizi et al. (12) for analysis of specificity; polyclonal rabbit anti-α2-subunit (1:1,000; Synaptic Systems); see Auferkorte et al. (13) for KO control; polyclonal rabbit anti–α3-subunit (1:500; Synaptic Systems); polyclonal guinea pig anti–γ2-subunit (1:1,000; Synaptic Systems) (14)] were incubated for 24 h at room temperature with 10% NGS and 0.2% Triton X-100 in PBS. After several rinses in PBS, slices were incubated for 24 h at room temperature with the secondary antibodies [goat anti-rabbit–Cy3 (1:500; Jackson ImmunoResearch Laboratories); goat anti-guinea pig–Alexa Fluor 647 (1:500; Invitrogen)] plus streptavidin–Alexa Fluor 488 conjugate (1:500; Invitrogen) with 10% NGS in PBS. Finally, slices were washed and embedded in Mowiol. Confocal images were taken with a Zeiss LSM710 confocal microscope and a Zeiss Plan-Apochromat 63× oil-immersion objective (N.A. 1.4).

We concentrated on α1- to α3-subunits for the following reasons: first, α1–α3 have been shown to be expressed in dentate gyrus GCs, coassembled with γ2-subunits to form predominantly postsynaptic $GABA_A$ receptors ($GABA_A$Rs) in these cells (15, 16). Second, α4- and α5-subunits are expressed in dentate gyrus GCs but form predominantly extrasynaptic $GABA_A$Rs, e.g., with the δ-subunit (15–18). Last, the α6-subunit seems to be absent from dentate gyrus GCs (15). Overall, these findings strongly indicate that $GABA_A$Rs containing γ2-subunits in association with α1, α2, or α3 are the predominant receptor type in dentate gyrus GCs that generate phasic postsynaptic inhibition (16). For automatic unbiased analysis of colocalization between axon and α1, α2, α3, or γ2 puncta (Fig. S6), two regions (100 × 100 × ~30 μm) were selected, one close to the PII soma (<100 μm) and one more remote (>200 μm). All somatic and dendritic structures of the labeled PII were manually removed from the biocytin channel in these regions. Both input channels, the biocytin channel and the respective receptor subunit channel, were thresholded to obtain binary images. In every z level, thresholds were individually calculated on the basis of the intensity histograms. The threshold for the biocytin channel was defined as 30× mean intensity, which almost only included axonal structures in the binary image. Thresholds of the immunostainings against $GABA_A$R subunits were chosen so that $(100 - X)$% of the brightest voxels (voxel size, 80 × 80 × 350 nm) in every z level were included in the receptor protein channels (default: X = 90%). Both binarized images were multiplied, resulting in a binary image stack in which the number of colocalized voxels was obtained for every z slice ($\mathrm{Voxels}_{\mathrm{colocalization}}$). To control for random colocalizations, 100 random versions of the input channels were created by

shuffling 10 × 10 voxel squares in every z slice and quantifying the number of colocalized voxels (mean: $\text{Voxels}_{\text{random}}$). For every z slice, colocalization was quantified as C_z:

$$C_z = \text{Voxels}_{\text{colocalization}} / \text{Voxels}_{\text{random}}. \quad \textbf{[S6]}$$

The total colocalization was the average of all C_z values for which $\text{Voxels}_{\text{colocalization}}$ was significantly larger in the original than in the random images. This difference was assumed to be significant if $\text{Voxels}_{\text{colocalization}}$ was larger than the 99th percentile of the random colocalizations.

Colocalization analysis was generally based on strict overlap of axonal and immunostainings. In theory, biocytin labels presynaptic and immunostainings label postsynaptic compartments of synaptic connections, which are separated by a defined distance of less than 50 nm (19). As the voxel size is above this resolution and antibody stains expand beyond the labeled structure, for the most part of the results we only use strict overlap of both channels. However, Fig. S6*C* shows the colocalization results after enlargement of the axonal structures by two voxels in every direction.

To normalize for differences in the local integrity of the slice and resulting staining quality differences between close and distant images, the colocalization of the α-subunits was always normalized to the colocalization of the γ2-subunit with the axon in the same image (Fig. S6*B*). To estimate the expression of the different α-subunits only in γ2-positive synaptic contacts (Fig. 3*C*), all voxels showing colocalization between γ2 and biocytin were tested for staining of the respective α-subunit. Image processing and analysis were done with Fiji based on ImageJ 1.47g and MATLAB.

Estimation of the Bouton Density in PII Axons. High-resolution confocal image stacks were obtained from intracellularly labeled PIIs. For every cell, six well-discernible axon collaterals (30–250 μm long) were reconstructed close (<100 μm) and distant (>200 μm) from the PII soma. Bouton-like varicosities were visually counted along these collaterals, and the average density for all analyzed collaterals was determined.

Pharmacological Manipulation of $GABA_A$ Receptor Kinetics. To test for differential subunit composition at perisomatic synapses originating from close vs. distant presynaptic PIIs, GCs were held in voltage clamp and compound IPSCs were evoked by extracellular stimulation in the GC layer. Glutamatergic and $GABA_B$ receptor-mediated signals were blocked by 4 mM kynurenic acid and 1 μM CGP35348, respectively. Two stimulation electrodes were used, one in close proximity to and one distant from the recorded GC. The distant stimulation site will recruit distant PII inputs, whereas the close stimulation site will activate fibers from both close and distant PIIs. To test for $GABA_A$ receptor subunit composition underlying the evoked IPSCs, 0.1–1 μM zolpidem was bath-applied and the modulatory effect was quantified.

Network Simulations. Interneurons (INs) contained a leak conductance of 0.13 $\text{mS}\cdot\text{cm}^{-2}$ and voltage-gated Hodgkin-Huxley–type Na^+ and K^+ conductances with a resting potential of −65 mV (20). Principal neurons (PNs) contained passive, voltage-gated Na^+, and three voltage-gated K^+ (delayed rectifier, A-type, and M-type) conductances to imitate the regular spiking phenotype of hippocampal PNs. The mechanisms were adapted from Hemond et al. (21). Their resting membrane potential was −75 mV.

Synaptic latencies consisted of a constant component of 0.5 ms plus a variable part scaling with the distance between presynaptic and postsynaptic cell. The variable part increased by 0.05 ms per PN distance. Every IN formed inhibitory connections with randomly chosen PNs at a mean connectivity of 80 connections (22). Connection probability dropped with distance in a Gaussian manner (SD = 25 cell-to-cell distances) following anatomical data (22). In the simulations with spatially restricted IN axons ("clipping"), connection probability was set to "0" at ≥10, ≥20, ≥30, or ≥40 cell-to-cell distances (clip 20%, 40%, 60%, or 80%, respectively; Fig. S9). Synapses were modeled conductance-based with properties deferred from our own experimental data. In the model without distance-dependence, unitary synaptic connections had the following properties: peak amplitude = 0.02 $\text{mS}\cdot\text{cm}^{-2}$, rise time constant τ_{RT} = 0.16 ms, and decay time constant τ = 7.0 ms. Reversal potential was set to E_{syn} = −65 mV (23). In the distance-dependent network, peak amplitude and decay time constant changed with the distance between presynaptic and postsynaptic neuron with the distance-dependence coefficients α = 0.5 ms^{-1} | β = 1.2 $\text{ms}\cdot\text{ms}^{-1}$ (Fig. 5*A*). These coefficients correspond to α and β in Eqs. **S1** and **S2**. The values for α and β in network simulations were below the experimentally defined parameters to account for the conversion from a 3D situation in the brain to the 1D model. We set boundaries to the distance-dependent parameters amplitude and τ (amp_∞ and τ_∞, amp_0 and τ_0) to keep values in a realistic range. Amp_∞ was set to $(0.1 \cdot \text{amp}_0)$ to ensure quantal transmission at every formed synapse and τ_∞ was defined as 13 ms, the largest τ measured at PII–GC synapses (Fig. 1*D*). The average strength and time course of inhibition critically influences network oscillations (24). Thus, in a first step, we adjusted τ_0 in the distance-dependent network so that the average τ of all inhibitory synapses matched τ = 7.0 ms, the default value of the non–distance-dependent network. Second, amp_0 was chosen to set the average inhibitory strength (conductance integral) in the distance-dependent network equal to the control model.

In each simulation run, PNs were launched with randomly distributed membrane resting potentials. Next, from t = 25 ms onward, INs were driven with highly correlated bursts of synaptic inputs arriving at different frequencies f_{drive}. At the same time, PNs received uncorrelated trains of Poisson-distributed excitatory synaptic events at, on average, 6,000 Hz with heterogeneous peak amplitudes (τ_{rise} = 0.1 ms, τ_{decay} = 2 ms, amplitude = 0.01 $\text{mS}\cdot\text{cm}^{-2}$, CV of amplitude = 0.2) to reproduce fast AMPA receptor-mediated inputs. At t = 150 ms, synapses were switched on. Between $200 \le t < 500$ ms, network activity was quantified.

To estimate the ability of the IN network to entrain randomly driven PNs, PN spikes were sampled and their time points were related to the closest peak of IN activity. Next, the SD of the resulting firing probability histogram for PNs was obtained (Fig. 5*C*, *Left*). To relate the shape of inhibition to the spiking behavior of PNs the total inhibitory conductance in the network (G) was monitored and subjected to a power spectral analysis using MATLAB's *periodogram* algorithm. The maxima of the resulting power spectra were used to calculate the G power at different f_{drive} levels (Fig. 5*D*, *Right*). All results are based on averages from 10 runs with random initial conditions.

Dynamic-Clamp Experiments. Compound inhibitory conductances were injected into GCs in real time by a single-electrode dynamic clamp (25, 26) driven by Signal 5.11 (Cambridge Electronic Design) in combination with a Power1401 mkII at a throughput rate of 50 kHz. Series resistance was constantly compensated by a bridge balance circuit (MultiClamp 700B; Axon Instruments). All recordings were performed at 32–34 °C in the presence of 5 μM SR95531 and 4 mM kynurenic acid to block $GABA_A$ receptor- and glutamate receptor-mediated synaptic transmission. Membrane potentials were filtered at 10 kHz and digitized by the ADC. We evoked trains of action potentials in GCs by injecting positive currents for 1.2 s with varying amplitude. Then, 0.1 s after the onset of the step depolarization, non–distance-dependent or distance-dependent compound conductance waveforms (G_{GABA}) were injected at different frequencies (f_{drive}) for the duration of 1 s. The artificial I_{GABA} was calculated by $I(t) = g(t) \times (V(t) - E_{GABA})$ with E_{GABA} = −65 mV (23). The shape of the injected compound

conductance resembled the inhibitory output of a synchronously spiking nodd and dd PII network model (Fig. 5 *A* and *B*). It was calculated as the sum of non–distance-dependent or distance-dependent unitary conductances originating from all PIIs in the network multiplied with the connection probability for the respective distance. Peak conductance of the nodd waveform was varied between 4 and 8 nS. The area under the conductance waveforms was always the same for nodd and dd inhibition within one GC recording. Individual experiments consisted of 30 sweeps with nodd, dd, and no inhibition in a randomly alternating fashion. Data points in Fig. 6*B* represent averages of all combinations of current injections for individual cells.

To determine timing and probability of action potential generation, individual spikes were sorted according to the oscillatory cycle they occurred in. For subsequent oscillatory cycles, we determined the spike time relative to the onset of inhibition, the SD of spike times, and their probability of occurrence. Due to the initial adaptation of GC discharges, data shown in Fig. 6*B* are average values obtained from the last 0.9 s of the step depolarization when adaptation was mild.

1. Freund TF, Buzsáki G (1996) Interneurons of the hippocampus. *Hippocampus* 6(4): 347–470.
2. Hosp JA, et al. (2014) Morpho-physiological criteria divide dentate gyrus interneurons into classes. *Hippocampus* 24(2):189–203.
3. Hu H, Martina M, Jonas P (2010) Dendritic mechanisms underlying rapid synaptic activation of fast-spiking hippocampal interneurons. *Science* 327(5961):52–58.
4. Kraushaar U, Jonas P (2000) Efficacy and stability of quantal GABA release at a hippocampal interneuron-principal neuron synapse. *J Neurosci* 20(15):5594–5607.
5. Barrett EF, Stevens CF (1972) The kinetics of transmitter release at the frog neuromuscular junction. *J Physiol* 227(3):691–708.
6. Minneci F, Kanichay RT, Silver RA (2012) Estimation of the time course of neurotransmitter release at central synapses from the first latency of postsynaptic currents. *J Neurosci Methods* 205(1):49–64.
7. Geiger JR, Lübke J, Roth A, Frotscher M, Jonas P (1997) Submillisecond AMPA receptor-mediated signaling at a principal neuron-interneuron synapse. *Neuron* 18(6):1009–1023.
8. Bucurenciu I, Bischofberger J, Jonas P (2010) A small number of open Ca^{2+} channels trigger transmitter release at a central GABAergic synapse. *Nat Neurosci* 13(1):19–21.
9. Hu H, Jonas P (2014) A supercritical density of Na^{+} channels ensures fast signaling in GABAergic interneuron axons. *Nat Neurosci* 17(5):686–693.
10. Helmchen F, Imoto K, Sakmann B (1996) Ca^{2+} buffering and action potential-evoked Ca^{2+} signaling in dendrites of pyramidal neurons. *Biophys J* 70(2):1069–1081.
11. Gao B, Fritschy JM, Benke D, Mohler H (1993) Neuron-specific expression of $GABA_A$-receptor subtypes: Differential association of the alpha 1- and alpha 3-subunits with serotonergic and GABAergic neurons. *Neuroscience* 54(4):881–892.
12. Patrizi A, et al. (2008) Synapse formation and clustering of neuroligin-2 in the absence of $GABA_A$ receptors. *Proc Natl Acad Sci USA* 105(35):13151–13156.
13. Auferkorte ON, et al. (2012) $GABA_A$ receptors containing the $\alpha 2$ subunit are critical for direction-selective inhibition in the retina. *PLoS One* 7(4):e35109.
14. Körber C, et al. (2012) Effects of distinct collybistin isoforms on the formation of GABAergic synapses in hippocampal neurons. *Mol Cell Neurosci* 50(3-4):250–259.
15. Wisden W, Laurie DJ, Monyer H, Seeburg PH (1992) The distribution of 13 $GABA_A$ receptor subunit mRNAs in the rat brain. I. Telencephalon, diencephalon, mesencephalon. *J Neurosci* 12(3):1040–1062.
16. Farrant M, Nusser Z (2005) Variations on an inhibitory theme: Phasic and tonic activation of $GABA_A$ receptors. *Nat Rev Neurosci* 6(3):215–229.
17. Wei W, Zhang N, Peng Z, Houser CR, Mody I (2003) Perisynaptic localization of delta subunit-containing $GABA_A$ receptors and their activation by GABA spillover in the mouse dentate gyrus. *J Neurosci* 23(33):10650–10661.
18. Brünig I, Scotti E, Sidler C, Fritschy J-M (2002) Intact sorting, targeting, and clustering of gamma-aminobutyric acid A receptor subtypes in hippocampal neurons in vitro. *J Comp Neurol* 443(1):43–55.
19. Klausberger T, Roberts JDB, Somogyi P (2002) Cell type- and input-specific differences in the number and subtypes of synaptic $GABA_A$ receptors in the hippocampus. *J Neurosci* 22(7):2513–2521.
20. Wang XJ, Buzsáki G (1996) Gamma oscillation by synaptic inhibition in a hippocampal interneuronal network model. *J Neurosci* 16(20):6402–6413.
21. Hemond P, et al. (2008) Distinct classes of pyramidal cells exhibit mutually exclusive firing patterns in hippocampal area CA3b. *Hippocampus* 18(4):411–424.
22. Sik A, Penttonen M, Ylinen A, Buzsáki G (1995) Hippocampal CA1 interneurons: An in vivo intracellular labeling study. *J Neurosci* 15(10):6651–6665.
23. Sauer J-F, Strüber M, Bartos M (2012) Interneurons provide circuit-specific depolarization and hyperpolarization. *J Neurosci* 32(12):4224–4229.
24. Bartos M, et al. (2002) Fast synaptic inhibition promotes synchronized gamma oscillations in hippocampal interneuron networks. *Proc Natl Acad Sci USA* 99(20): 13222–13227.
25. Prinz AA, Abbott LF, Marder E (2004) The dynamic clamp comes of age. *Trends Neurosci* 27(4):218–224.
26. Vida I, Bartos M, Jonas P (2006) Shunting inhibition improves robustness of gamma oscillations in hippocampal interneuron networks by homogenizing firing rates. *Neuron* 49(1):107–117.

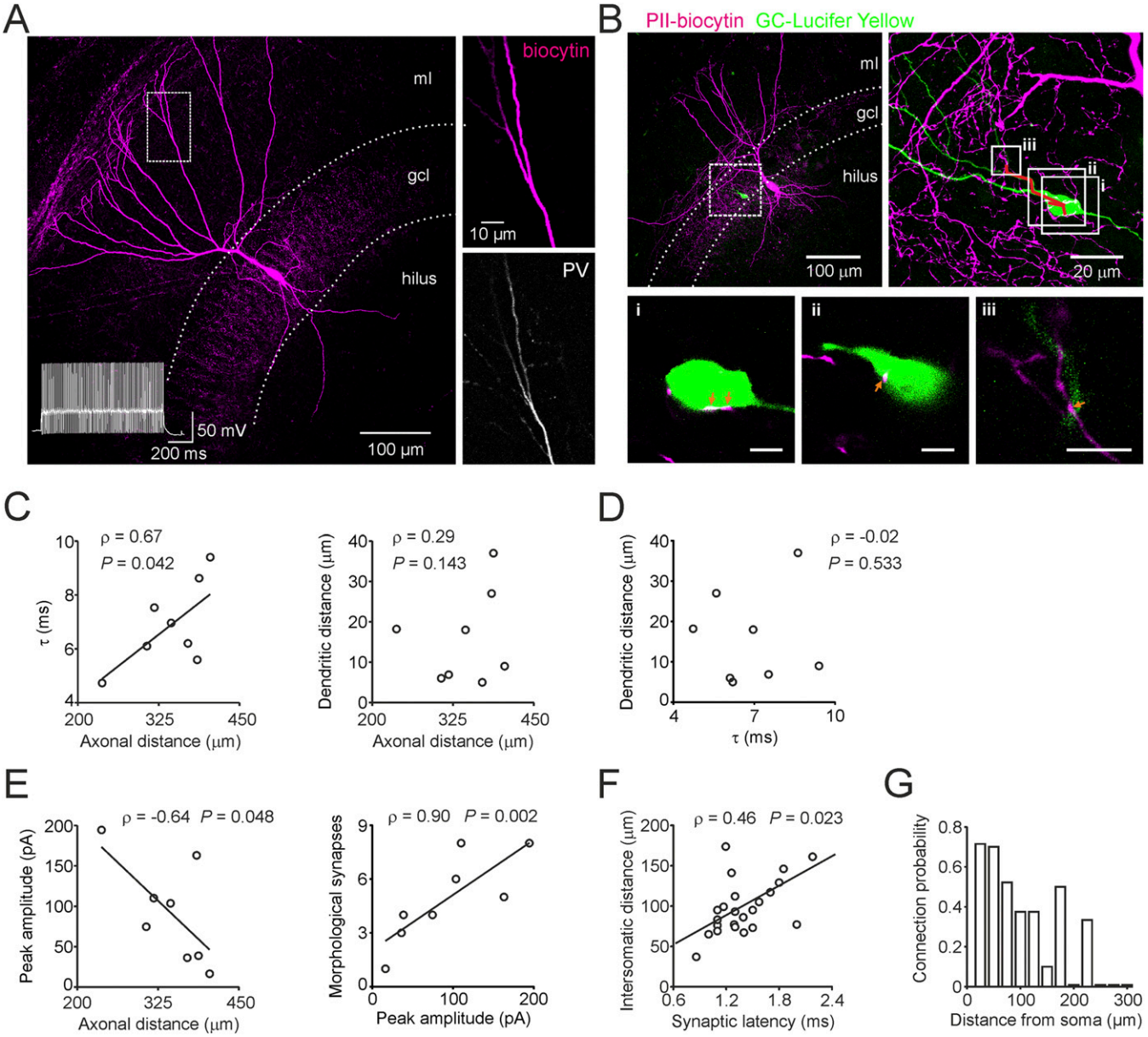

Fig. S1. Morphological characterization of PII–GC connections. (*A*, *Left*) Intracellularly labeled PII with its axon restricted to the granule cell layer (gcl) fires high-frequency action potentials in response to 350-pA current injection (*Inset*). (*Right*) Dendrite shows expression of the Ca^{2+} binding protein parvalbumin (PV). Magnification of the box shown *Left*. (*B*, *Top*) Maximum intensity projections of confocal image stacks of a PII–GC pair. The PII was intracellularly filled with biocytin, and the GC, with Lucifer Yellow. Box in left panel is shown at higher magnification in the right panel. Red lines in the right panel illustrate dendritic distances from three putative synaptic contact sites to the center of the GC soma (green). These four putative synapses are shown at higher magnification as single confocal images in *i–iii* (*Bottom*). Arrows indicate putative contacts. (Scale bar: 4 µm.) (*C–E*) Data from eight reconstructed PII–GC pairs. (*C*, *Left*) Decay time constant (τ) of uIPSCs. (*Right*) Dendritic distance plotted against axonal distance. Note that synapse location cannot explain distance-dependent differences in τ of uIPSCs. (*D*) Dendritic distance is not correlated with the decay time constant (τ) of uIPSCs. (*E*, *Left*) uIPSC peak amplitude correlates with axonal distance in reconstructed PII–GC pairs. (*Right*) Number of putative contact sites correlates with uIPSC peak amplitudes (Fig. 1*F*). (*F*) Intersomatic distance of PII–GC pairs plotted as a function of synaptic latency (Fig. 1*C*). (*G*) The probability to obtain a connected PII–GC pair drops with the distance from the PII soma. Lines are linear fits to the data. ρ, Spearman's rank correlation coefficient; *P* values in *C–F* result from one-tailed correlation analysis.

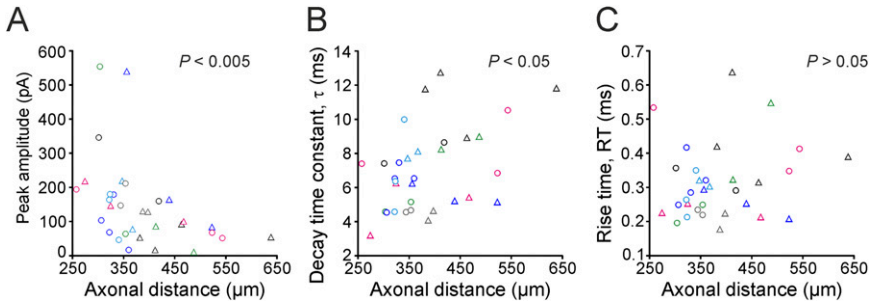

Fig. S2. Multiple sequential paired recordings (SPRs) reveal distance-dependence of inhibitory signaling at PII–GC synapses. (*A–C*) uIPSC parameters [peak amplitude (*A*), τ (*B*), and 20–80% rise time (RT) (*C*)] from sequential PII–GC recordings. A paired recording was first established. The postsynaptic pipette was removed and a second GC was patched while the presynaptic PII was kept the same. This procedure was usually repeated four to six times. Data recorded from one presynaptic PII and its several postsynaptic GCs are depicted by one color either as circles or as triangles (32 PII–GC pairs in 12 sets of sequential paired recordings; Fig. 1*D*). *P* values indicate statistically significant relationships of amplitude and τ with axonal distance for individual SPRs (*SI Materials and Methods*).

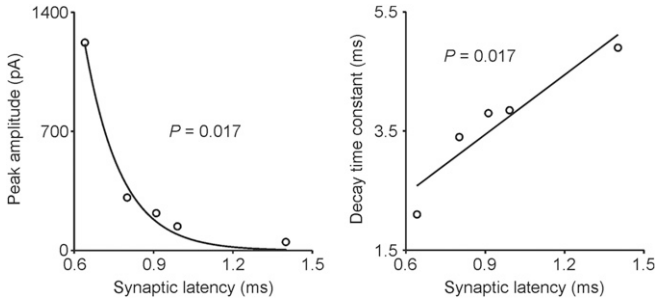

Fig. S3. Distance-dependence in CA1 PII–pyramidal cell paired recordings. uIPSC peak amplitudes (*Left*) and decay time constants (*Right*) of five CA1 PII–pyramidal cell paired recordings are plotted against the respective synaptic latency. Similarly to the dentate gyrus, the amplitude of perisomatic inhibition declines with larger latencies while its duration becomes longer. *P*, Spearman's correlation analysis.

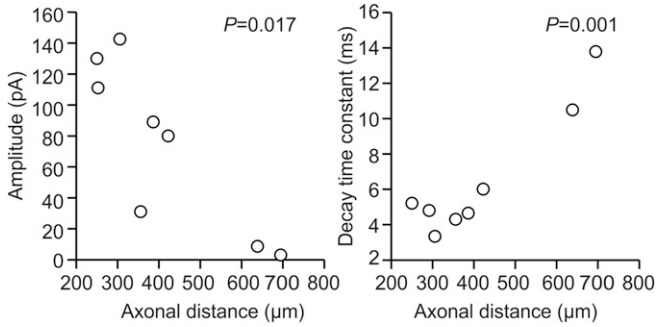

Fig. S4. Distance-dependent inhibition in adult dentate gyrus PIIs. PII–GC paired recordings were performed in hippocampal slices of 30- to 45-d-old rats. Both average uIPSC peak amplitudes (*Left*) and decay time constants (*Right*) are plotted against distance and show a clear distance-dependent change ($P = 0.017$ and $P = 0.001$; Pearson product correlation; amplitude and τ, respectively; eight pairs).

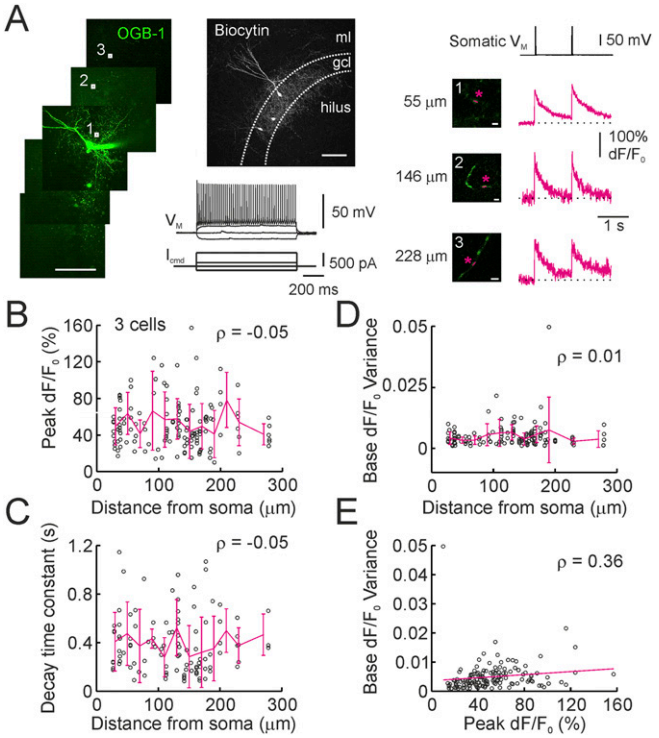

Fig. S5. Properties of spike-induced presynaptic Ca^{2+} signals do not change along PII axons. (*A*) A PII was intracellularly filled with 100 μM OGB-1 (*Left*) and 1 mg·mL^{-1} biocytin for post hoc visualization (*Top Middle*). (*Bottom Middle*) Characteristic fast-spiking firing pattern of the same cell. (*Right*) Ca^{2+} transients (magenta traces) in response to two somatically evoked single action potentials (top trace) could be reliably recorded in putative boutons using two-photon imaging at different positions along the axonal arbor. Black dotted line indicates the prestimulus baseline. Numbered boxes refer to axon location magnified in the *Insets*. Magenta lines and asterisks in *Insets* indicate location of the line scans. [Scale bars: 100 μm (*Left* and *Top Middle*); 2 μm (*Insets*).] (*B–E*) Peak (*B*) and decay time constants (*C*) of the fluorescence change (dF/F_0) are plotted as a function of distance from the PII soma. Variance of the preceding baseline (*D* and *E*) does not correlate with distance, but with the peak of action potential-induced Ca^{2+} transients. Individual circles show pooled data from three PIIs. Magenta lines with error bars represent mean ± SD of the pooled data (ρ, Spearman's correlation coefficient). Both the peak dF/F_0 and the decay time constant do not change with the bouton distance from the soma (*B* and *C*; $P = 0.547$ and $P = 0.615$, respectively), suggesting that presynaptic Ca^{2+} transients are uniform throughout the whole PII axonal arbor. The baseline noise (*D*; $P = 0.872$) is homogeneous over the axon indicating equal dye distribution. *E* shows the expected relationship between baseline noise and peak dF/F_0 ($P < 0.001$) (1).

1. Maravall M, Mainen ZF, Sabatini BL, Svoboda K (2000) Estimating intracellular calcium concentrations and buffering without wavelength ratioing. *Biophys J* 78(5):2655–2667.

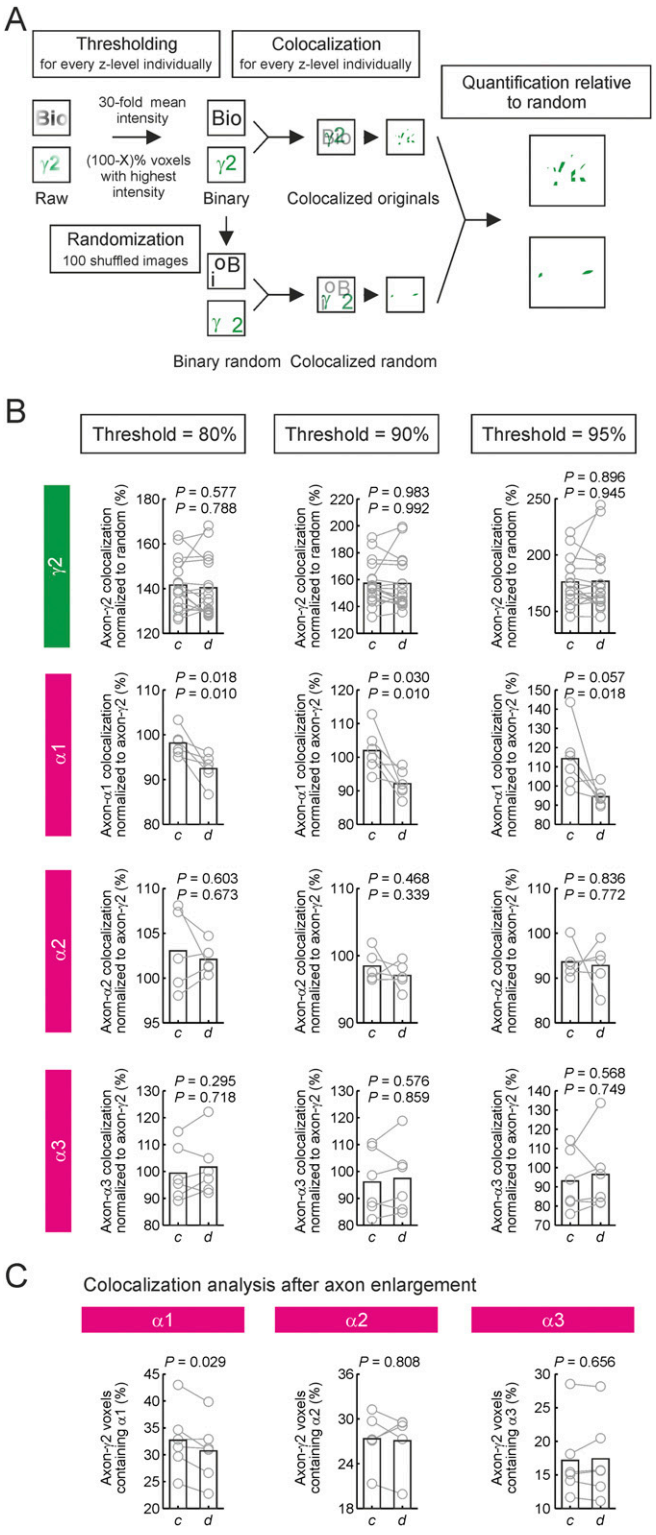

Fig. S6. Expression of the $GABA_AR$ subunit α1 declines with distance at PII axons. (*A*) Flowchart illustrating colocalization analysis of biocytin-filled axon and immunostainings against $GABA_AR$ subunits α1, α2, α3, and γ2 (*SI Materials and Methods*). (*B*) Results of the colocalization analysis between biocytin-filled axon and receptor subunits for three different thresholds for the receptor subunits (80%, 90%, and 95%; *X* in *A*). All α-subunit colocalizations are normalized to the γ2 colocalization in the same image. Upper *P* values, paired *t* test; lower *P* values, unpaired *t* test. Abbreviations: *c*, close (<100 μm to PII soma); *d*, distant (>200 μm to PII soma). (*C*) Analysis of α-subunit content in γ2-positive axon voxels after enlargement of the thresholded biocytin-filled axon by two voxels in every direction.

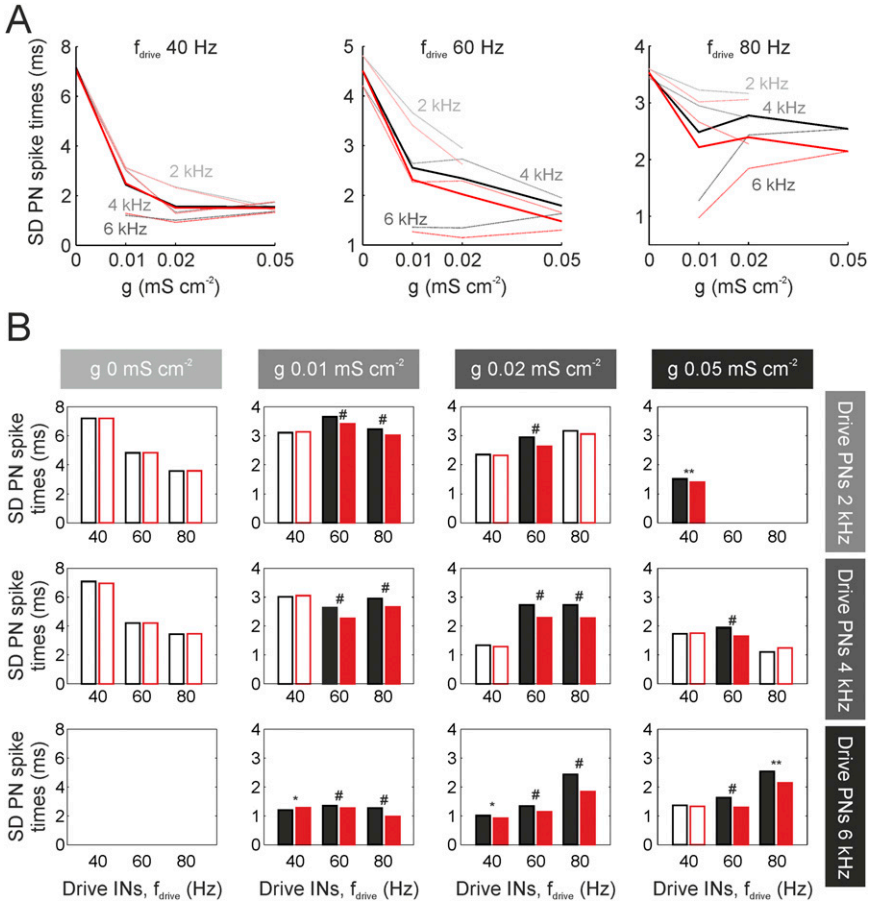

Fig. S7. Improved entrainment of principal neurons (PNs) with distance-dependent inhibition is robust against variations in the details of the network model. (*A*) Spike timing of PNs quantified as the SD of spike times plotted against the unitary conductance (*g*) at IN–PN synapses at three different excitatory drives onto PNs of 2, 4, and 6 kHz and three different excitatory drives onto INs (f_{drive}) at frequencies of 40, 60, and 80 Hz (*Left*, *Middle*, and *Right*, respectively). Thin lines represent simulation results at different PN excitation levels, and bold lines represent average data. Black, no distance-dependence; red, distance-dependent network model. Note the lower SD of spike timing in PNs in the distance-dependent model at 60 and 80 Hz. (*B*) Bar graphs summarize SD of PN spike timing at three different excitatory drives onto INs (f_{drive}), four unitary inhibitory conductances at IN–PN synapses (*g*; 0–0.05 mS·cm^{-2}), and three different excitatory drives (2–6 kHz) onto PNs. Red bars represent data from distance-dependent and black bars from distance-independent models. Open bars indicate lack of statistical difference, and filled bars show a difference between both networks (*$P < 0.05$; **$P < 0.01$; $^{\#}P < 0.001$). Absence of bars in *B* and data points in *A* is due to inactivation of PN Na^+ conductances at 0 inhibitory conductance or silencing of PNs due to high inhibitory conductance (0.05 mS·ms^{-2}). Note that the precision of spike timing of PNs in the distance-dependent network is significantly higher than in the non–distance-dependent model if realistic inhibitory conductances (0.01–0.02 mS·cm^{-2}) (1) were included in the model.

1. Bartos M, Vida I, Frotscher M, Geiger JR, Jonas P (2001) Rapid signaling at inhibitory synapses in a dentate gyrus interneuron network. *J Neurosci* 21(8):2687–2698.

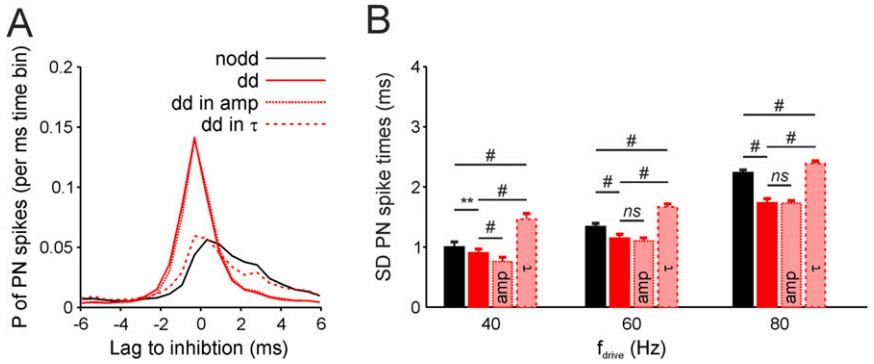

Fig. S8. Differential influence of distance-dependent amplitude and time course of inhibition. (*A*) Average spike time histograms of PNs receiving rhythmic inhibition (f_{drive} = 80 Hz) from INs providing uniform (nodd, black) or distance-dependent inhibition (dd, red). The distance-dependence is implemented in either amplitude (dd in amp, red dotted line) or decay time constant (dd in τ, red dashed line) or in both properties (dd, red continuous line). All spike times are indicated relative to maximal IN discharge in the respective oscillation cycle (Fig. 5). (*B*) Quantification of spike time precision as the SD of all PN spikes relative to maximal IN discharge in every oscillation cycle. Note that the positive influence of distance-dependent inhibition on PN entrainment by PIIs is mainly due to the distance-dependent distribution of uIPSC amplitudes. All data are averages from 10 runs. $^{**}P < 0.01$; $^{\#}P < 0.001$; *ns*, not significant.

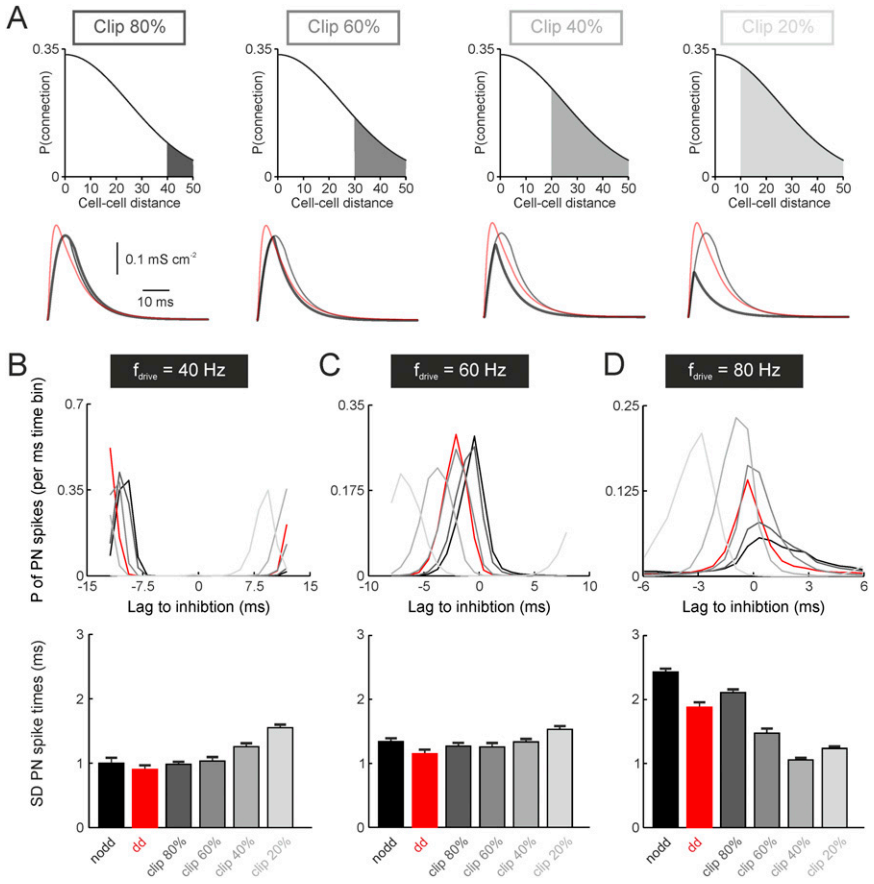

Fig. S9. Clipping the IN axon at different distances improves entrainment at high- but impairs synchrony at low-gamma frequencies. (*A*, *Top*) Connection probabilities for PII–PN synapses for different clipping scenarios (from *Left* to *Right*, clipping occurs at 80%, 60%, 40%, or 20% of the original maximal projection distance). (*Bottom*) Average compound conductance recorded from a PN after synchronous spiking of a nodd (thin gray line), dd (red), or $nodd_{clipped}$ (bold gray line) PII network. (*B–D*, *Top*) Average spike time histograms of PNs entrained by rhythmically active INs at 40- (*B*), 60- (*C*), and 80-Hz (*D*) oscillation frequency. (*Bottom*) Quantification of the spike timing precision of PNs. Model INs provided either uniform (nodd, black) or distance-dependent inhibition (dd, red). Different gray values indicate the spatial extent of the IN axon after clipping at 20–80% of the original extent. All clipped INs provided distance-independent synaptic inhibition.